

Article

Experimental and Simulation Studies on Stable Polarity Reversal in Aged HVDC Mass-Impregnated Cables

Sun-Jin Kim, Seol Lee, Woo-Sung Choi and Bang-Wook Lee * 

Department of Electronic Engineering, Hanyang University, Ansan 15588, Republic of Korea; ksj8119@hanyang.ac.kr (S.-J.K.); zmffkdnem13@hanyang.ac.kr (S.L.); sung1108@hanyang.ac.kr (W.-S.C.)

* Correspondence: bangwook@hanyang.ac.kr; Tel.: +82-31-400-4752

Abstract: Mass-impregnated (MI) cables have been used for many years as cables in high-voltage direct current (HVDC) systems. In line commutated converter (LCC) HVDC systems, polarity reversal for power flow control can induce significant electrical stress on MI cables. Furthermore, the mass oil and kraft paper comprising the impregnated insulation have significantly different coefficients of thermal expansion. Load fluctuations in the cable lead to expansion and contraction of the mass, creating pressure within the insulation and causing redistribution of the impregnant. During this process, shrinkage cavities can form within the butt gaps. Since the dielectric strength of the cavities is lower than that of the surrounding impregnation, cavitation phenomena in impregnated paper insulation are considered a factor in degrading insulation performance. Consequently, this study analyzes the electrical conductivity of thermally aged materials and investigates the transient electric field characteristics within the cable. Additionally, it closely analyzes the formation and dissolution of cavities in MI cables during polarity reversal based on a numerical model of pressure behavior in porous media. The conductivity of the impregnated paper indicates that it has excellent resistance to thermal degradation. Simulation results for various load conditions highlight that the interval of load-off time and the magnitude of internal pressure significantly influence the cavitation phenomenon. Lastly, the study proposes stable system operation methods to prevent cavitation in MI cables.

Keywords: HVDC cables; cable insulation; finite element analysis; impregnated insulation; thermal aging; electrical conductivity



Citation: Kim, S.-J.; Lee, S.; Choi, W.-S.; Lee, B.-W. Experimental and Simulation Studies on Stable Polarity Reversal in Aged HVDC Mass-Impregnated Cables. *Energies* **2024**, *17*, 2352. <https://doi.org/10.3390/en17102352>

Academic Editor: Nicu Bizon

Received: 15 April 2024

Revised: 10 May 2024

Accepted: 11 May 2024

Published: 13 May 2024



Copyright: © 2024 by the authors. Licensee MDPI, Basel, Switzerland. This article is an open access article distributed under the terms and conditions of the Creative Commons Attribution (CC BY) license (<https://creativecommons.org/licenses/by/4.0/>).

1. Introduction

High-voltage direct current (HVDC) systems are very advantageous for long-distance power transmission with high capacity and low losses [1–4]. Several HVDC projects aimed at connecting islands, nations, and continents are currently underway. Before the development of extruded cross-linked polyethylene (XLPE) insulation for HVDC, mass-impregnated (MI) cables were the most commonly used [5–7]. The insulation layer of the MI cable is made of kraft paper impregnated with a high-viscosity oil known as ‘mass’ and is constructed by wrapping around 200 layers of paper to form an electrical insulation system, achieving a total thickness of approximately 2–3 cm.

Compared to XLPE cables, MI cables offer the significant advantage of withstanding polarity reversal in Line Commutated Converter (LCC) HVDC systems, primarily due to their low space charge accumulation. This characteristic leads to less distortion in the internal electric field, enhancing the system’s reliability [8–10]. Owing to these stable electrical properties, MI cables have been extensively utilized in numerous LCC-HVDC systems for years and remain effective in current applications. However, given that MI cables initially installed in HVDC systems have been operational for over 20 years, we cannot overlook the potential for insulation material degradation. The requirements for polarity reversal and the on/off operations of loads for power flow control in LCC-HVDC systems can lead to localized enhancement of the electric field and stress accumulation, potentially causing

partial discharge within the cable insulation. In particular, if considering reversing the direction of power flow to distribute electricity produced from renewable energy sources to high-demand areas, it is critical to assess the safety of long-operated MI cables during polarity reversal [11]. Therefore, it is necessary to understand the characteristics of the MI paper insulation and review potential risk factors in advance.

A distinctive feature of MI cable insulation is that the coefficient of thermal expansion for mass oil is about 10 times greater than for kraft paper, indicating significantly different thermal behaviors between the two materials [12]. Thermal expansion and contraction of the mass oil due to load fluctuations or interruptions result in a pressure gradient within the insulation, leading to the redistribution of the impregnant. In particular, when the cable cools down after load disconnection, the contraction of the oil within the butt gaps and its increased viscosity prevent the displaced mass from returning, thereby creating cavities within the insulation [13]. These cavities have a lower dielectric strength compared to the surrounding insulation, which can lead to partial discharges when exposed to high electric fields. Notably, studies [14,15] have shown an increase in the recurrence rate of partial discharges for a period after the load is turned off. These observations support the widely accepted theory that the cavitation phenomenon, characterized by the formation of shrinkage cavities in the insulation during the cooling cycle after a load decrease or disconnection, substantially undermines cable integrity. Recent studies have reported on the measurement and numerical modeling of internal pressure under various temperature and pressure conditions in HVDC MI cable samples [16–18]. The findings demonstrate that rapid load changes increase the internal pressure within the insulation and induce mass flow. Moreover, the results of numerical models based on Darcy's law for internal pressure behavior have confirmed similarities with the measured outcomes. Additionally, our prior research has explored the partial discharge characteristics of impregnated insulation paper containing voids, revealing a reduction in the partial discharge inception voltage (PDIV) of aged insulation [19,20].

As previously described, ensuring the safe operation of MI cables in transient states, such as polarity reversal and load current disconnection, requires comprehensive evaluations of the potential risk factors. Consequently, measurements of activation energy needed for accelerated aging tests of impregnated paper and the selection of aging durations were initially conducted. Following this, we analyzed the electrical conductivity of the materials and applied these parameters to an electric field analysis model. Simulations were conducted to identify changes in the internal electric field characteristics of the cable under transient conditions, with a numerical model incorporating mass flow to specifically focus on the formation and dissolution of cavities within the insulation. The internal pressure profile was derived by varying the polarity reversal timing and load-off conditions. Finally, we identified the most critical factors influencing the cavitation phenomenon in MI cables and proposed suitable operational methods for polarity reversal actions based on the simulation results.

2. Experimental Methods

2.1. Specimen Preparation

The specimens used in the experiment consisted of kraft paper impregnated with mass oil. Given the high viscosity of mass oil at low temperatures, it was necessary to increase the temperature and apply a vacuum to reduce the viscosity and ensure thorough permeation of the oil into the paper. Therefore, the impregnation process was carried out in a vacuum oven, set at a temperature of 70 °C and a pressure of –1 bar, for seven days.

2.2. Thermally Accelerated Degradation Tests

It would be ideal to conduct experiments on materials that naturally deteriorate in real environments, but this is often impractical due to the difficulty in obtaining sufficient samples and the extensive time required. However, accelerated degradation tests can estimate changes in material properties by subjecting insulation materials to conditions

more severe than those encountered in actual use. In this study, a thermally accelerated degradation test was performed on impregnated paper using a constant stress method among various thermal stress application methods.

For the thermally accelerated degradation method, the Arrhenius model, which describes the relationship between temperature and chemical reaction rates, is used. This is expressed in Equation (1). By taking the natural logarithm of both sides of Equation (1) and applying different temperature conditions, T_1 and T_2 , it can be reformulated as Equation (2).

$$K = A \exp\left(-\frac{E_a}{k_B T}\right) \quad (1)$$

$$K_1 = \frac{K_2}{\exp\left(\frac{E_a}{k_B}\left(\frac{1}{T_2} - \frac{1}{T_1}\right)\right)} \quad (2)$$

where K is the rate constant, A represents the pre-exponential factor, E_a is the activation energy, T denotes absolute temperature, and k_B is the Boltzmann constant. K_1 is the time for accelerated degradation, K_2 is the equivalent lifetime, T_1 is the temperature for accelerated degradation, and T_2 is the operational temperature. To select feasible degradation times and temperatures, as well as to achieve the desired equivalent lifetime, it is essential to first measure the activation energy.

Activation energy generally refers to the energy required by materials to initiate a chemical reaction. The higher the activation energy, the more energy is needed from external sources, making the reaction less likely to occur. Methods for measuring activation energy include Differential Scanning Calorimetry (DSC), which measures the heat flow in and out of a sample as it is heated and cooled alongside a reference material, and Thermogravimetric Analysis (TGA), which records changes in the sample's weight in response to temperature changes and measures these as a function of temperature. TGA is widely used and includes various analytical techniques. In this study, the Kissinger method was employed to measure the activation energy of the impregnated paper. The equipment used for the measurements was the SDT Q600 from TA Instruments, and nitrogen gas was utilized for the analysis. The heating rates were set at 10, 20, and 30 °C/min, reaching up to 600 °C. The maximum differential value in the weight loss from the Derivative Thermogravimetry (DTG) Curve obtained through analysis was used to calculate the activation energy by applying it to Equation (3) of the Kissinger method [21].

$$\frac{d(\ln \beta / T_m^2)}{d(1/T_m)} = -\frac{E_a}{R} \quad (3)$$

where β represents the heating rate, R is the universal gas constant (8.3136 J/(mol·K)), and T_m denotes the temperature at which the material's weight loss rate peaks.

2.3. Measurement of Leakage Current to Determine Electrical Conductivity

The leakage current of the impregnated paper was measured to analyze changes in its electrical properties over accelerated aging time and to use these measurements as parameters for the electric field analysis. To calculate the volume conductivity, the specimen was mounted between the top electrode and the main electrode as shown in Figure 1. When a high voltage is applied to the electrodes, the leakage current within the volume of the specimen is measured through the main electrode using a current meter (Keithley 6517b). Any leakage current that flows over the surface of the specimen or beyond the radius of the main electrode is diverted by a grounded ring-shaped guard electrode. Since volume conductivity is the inverse of volume resistivity, it can be calculated using Equation (4):

$$\sigma = \frac{1}{\rho_v} = \frac{I l}{V S} \quad (4)$$

where ρ_v denotes the volume resistivity, S denotes the area of the main electrode, I is the leakage current, V is the applied voltage, and l is the thickness of the kraft paper, 140 μm . Leakage current for both unaged and aged specimens was measured under three temperature settings (20 $^{\circ}\text{C}$, 35 $^{\circ}\text{C}$, 50 $^{\circ}\text{C}$) and three applied voltage levels (10 kV/mm, 12.5 kV/mm, 15 kV/mm) to calculate their volume conductivity. The conductivity values for each set of conditions were fitted to an electrical conductivity, Equation (5), that accounts for temperature and electric field dependencies. These fitted expressions were then used in the electric field analysis.

$$\sigma = \sigma_0 \exp(\alpha(T - T_0) + \gamma(E - E_0)) \quad (5)$$

where T is temperature, E the electric field, T_0 is the reference temperature (293.15 K), E_0 the reference electric field (10 kV/mm), σ_0 is the reference conductivity, and α and γ are the temperature and electric field dependent coefficients, respectively.

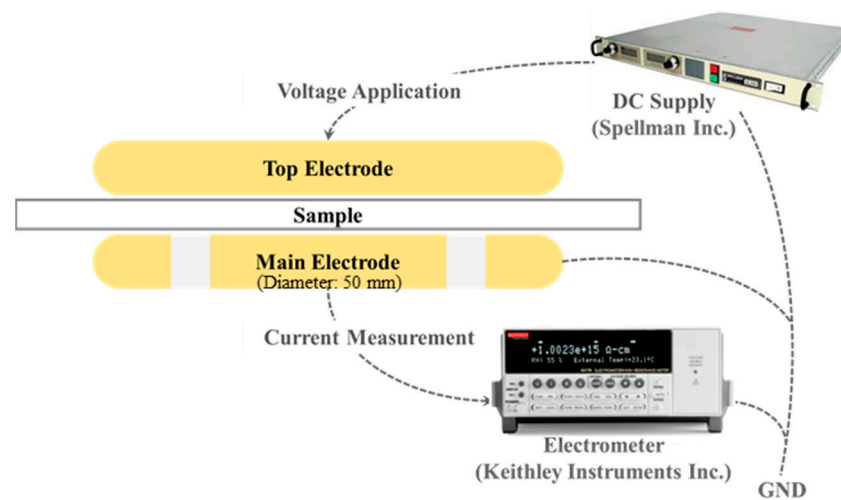


Figure 1. The schematic of leakage current measurement.

3. Experimental Results and Discussion

3.1. Activation Energy and Equivalent Lifetime Calculation

Figure 2a displays the DTG curves of impregnated paper with different heating rates and a fixed flow of nitrogen gas. Table 1 presents the data analyzed from the DTG graphs. Equation (3) can be reformulated as Equation (6), where the y -axis is $\ln\left(\frac{\beta}{T_m^2}\right)$ and the x -axis is $\frac{1}{T_m}$.

$$\ln\left(\frac{\beta}{T_m^2}\right) = -m\left(\frac{1}{T_m}\right) + b \quad (6)$$

where m and b represent the slope and intercept of the linear regression fitted to the data, respectively. As shown in Figure 2b, the data enable the derivation of a trend line. Since the slope m represents $\frac{E_a}{R}$, the activation energy is calculated to be 137.23 kJ/mol. Subsequently, this value was substituted into Equation (2) to determine the accelerated aging time. The aging temperature (T_1) and operating temperature (T_2) were set at 85 $^{\circ}\text{C}$ and 50 $^{\circ}\text{C}$, respectively, to achieve an equivalent lifetime of 30 years, corresponding to an aging duration of 1800 h (75 days).

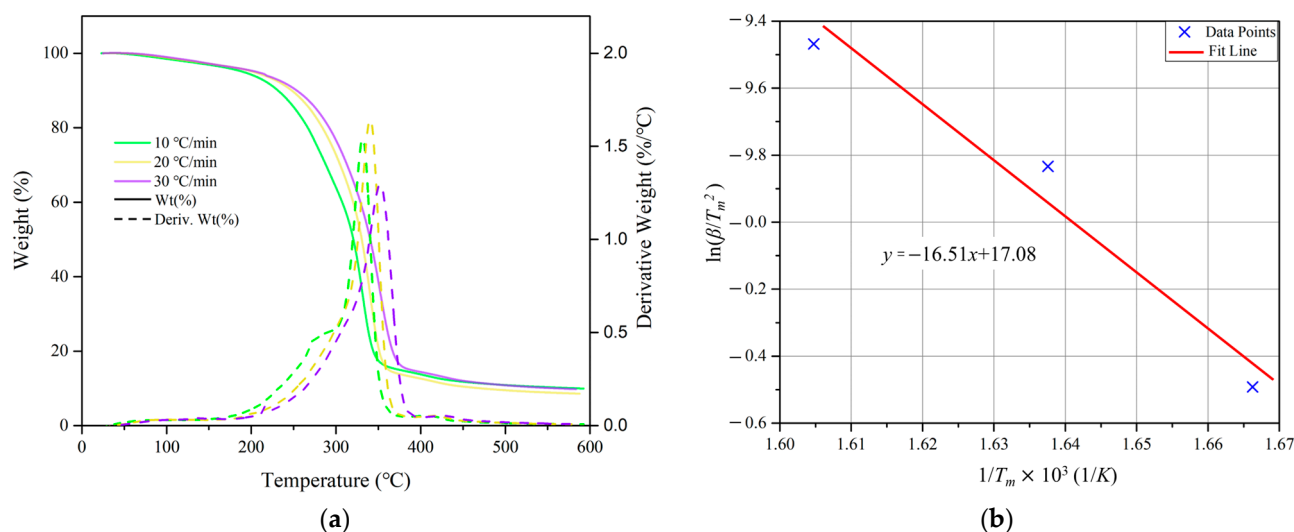


Figure 2. TGA results for activation energy derivation: (a) DTG curves; (b) Modified Kissinger plot.

Table 1. The parameters derived from DTG curves.

Heating Rate (°C/min)	T_m (K)	$(1/T_m) \cdot 10^3$ (1/K)	$\ln(\beta/T_m^2)$
10	600.15	1.66625	−10.491774
20	610.65	1.637599	−9.833316
30	623.15	1.60475	−9.468377

3.2. Electrical Conductivity

Figure 3a,b each display the leakage current and electrical conductivity of the specimens under different temperature and electric field conditions. The conductivity formula, which includes dependency coefficients, is presented in Figure 3b. The experiments showed that aged specimens exhibited an increase in leakage current compared to unaged ones.

Particularly under conditions of 50 °C and an electric field strength of 25 kV/mm, a noticeable difference in the leakage currents between the two specimens was observed compared to other conditions. At 20 kV/mm, the difference in leakage currents between the two specimens is approximately 0.5 nA, but at 25 kV/mm, it increases to about 1.6 nA. The phenomenon of increased leakage currents in the aged specimen beyond a certain electric field can be explained by the theory of space charge limited current (SCLC) [22]. SCLC theory describes the relationship between current density and voltage (or electric field) applied to dielectrics. The SCLC theory distinguishes between the Ohmic region ($J \propto V$) and the trap-limited SCLC region ($J \propto V^2$) based on the threshold electric field. The increased current density observed in the aged specimen at a temperature of 50 °C and an electric field of 25 kV/mm suggests that it may be entering the onset of the trap-limited region. There is also a possibility that the leakage current could increase significantly if the applied voltage is further increased under these temperature conditions. However, wider range measurements of leakage current were not performed due to the limitations of the measuring equipment. Nonetheless, a temperature of 50 °C represents the maximum permissible temperature for MI cables and is considered the severe condition. Under other temperature conditions, the differences in leakage current values and increases between the two specimens are not pronounced. Therefore, it is anticipated that, except under specific conditions, the insulation performance of the aged paper will remain effective during normal cable operation.

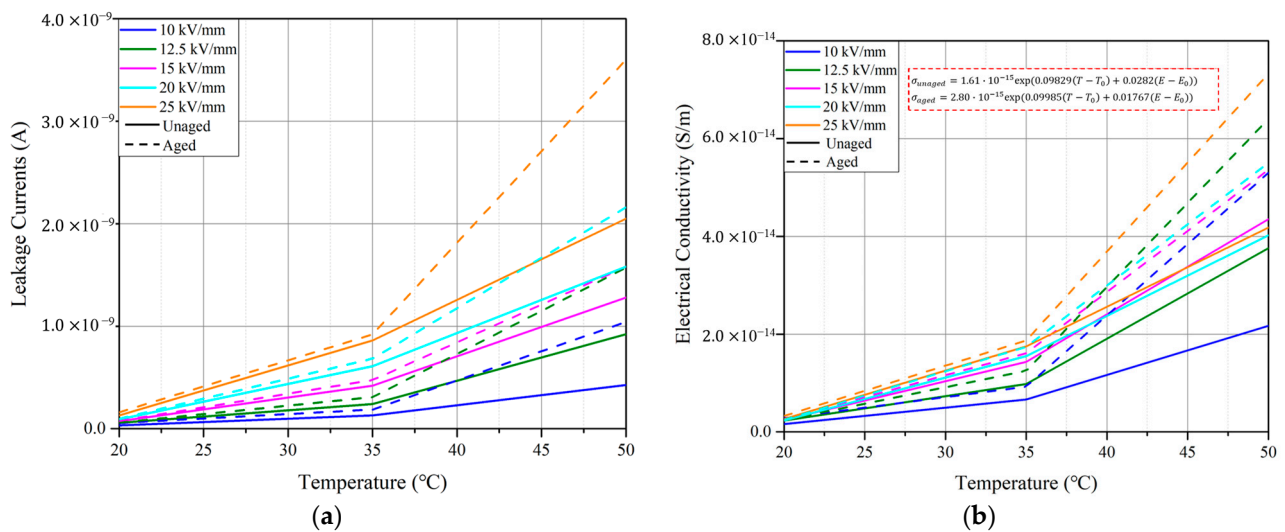


Figure 3. Leakage current measurement results under varying temperature and electric field conditions: (a) leakage current; (b) electrical conductivity.

Moreover, considering conductivity values in the range of 10^{-15} to 10^{-14} S/m, it is evident that the insulation performance remains effective even at aging intensities corresponding to a 30-year equivalent lifetime. This indicates the excellent resistance of mass impregnated papers to thermal degradation [23]. However, changes in dependent coefficients could alter the electric field distribution, necessitating a review of the internal field through simulation.

Additionally, the presence of cavities in the impregnated paper can lead to localized electric field concentration, potentially resulting in partial discharges. In aged materials, partial discharges may occur at lower electric field strengths [20]. Thus, even if there is no significant decline in the insulation performance of the material due to long-term use, the cavities inherent in the structural characteristics of MI cable insulation can degrade the overall insulation performance. Therefore, it is necessary to assess the suitability of MI cables for polarity reversal operations not only in terms of transient electric fields, but also from the perspective of cavity formation within the cable insulation, using numerical pressure analysis.

4. Simulation Models and Conditions

The finite element model was solved using COMSOL Multiphysics to obtain the electric field, temperature, and pressure inside the MI cable, accounting for the transient electric field and load variations during polarity reversal. COMSOL Multiphysics 6.1 is an advanced numerical simulation software that captures the essential physics needed to model dynamic changes in designed systems. In our numerical model, a 1D axisymmetric structure was employed to replicate the cable shape. For the MI cable 1D model, a highly nonlinear Newton solver setup was utilized to balance computation time and accuracy. The Newton–Raphson method, used for solving nonlinear equations, estimates the zero of a function via iterative linear system approximation. In this study, it was applied to identify sections of electric field concentration, pressure drop points, and to evaluate the risk of insulation breakdown considering the nonlinear characteristics of the dielectrics.

Electric field simulations were conducted using the Multi-frontal Massively Parallel Sparse Direct Solver (MUMPS). The MUMPS employs multiple independent frontal solvers to simultaneously address sparse matrices. Pressure simulations utilized the Parallel Direct Solver (PARADISO), which enhances the efficiency of solving large matrix problems by optimizing sparse matrix structures. In this paper, time-dependent simulations were applied to model the electric field and pressure distribution. The solver's time step was meticulously controlled to prevent issues in pressure calculations due to load variations.

The maximum number of iterations was set to four for the electric field analysis and eight for the pressure analysis, with tolerances set at 0.01 for the electric field analysis and 0.005 for the pressure analysis, ensuring result accuracy.

4.1. DC Electric Field Analysis

It is well-known that the calculation of the field in HVDC cables differs significantly from HVAC cables [24–26]. The electric field in an AC cable is determined solely by the cable structure, permittivity, and applied voltage and is referred to as the capacitive field. The DC field, on the other hand, depends on the electrical conductivity of the insulation, which has a temperature and field dependence, and is referred to as the resistive field. When joule heat is generated by a load current, a temperature gradient is created inside the insulation. This gradient alters a difference in conductivity along the insulation radius, which results in a build-up of space charge inside the insulation and a distortion of the electric field. As the dielectric reaches DC steady state, the field on the conductor side decreases and the field on the sheath side increases, causing a transition from a capacitive to a resistive field. Conduction and space charge accumulation within the HVDC field are governed by the equations outlined below.

$$J = \sigma E + \frac{\partial D}{\partial t} \quad (7)$$

$$\nabla \cdot J = -\frac{\partial \rho}{\partial t} \quad (8)$$

$$E = -\nabla V \quad (9)$$

$$\nabla \cdot (\varepsilon_0 \varepsilon_r E) = \rho \quad (10)$$

where J is the current density, ρ is the charge density, and D is the electric flux density.

Assuming no initial charge in the dielectric, the charge density remains zero when DC voltage is first applied, as indicated in Equation (11). Consequently, the initial electric field distribution is determined by the permittivity. With prolonged DC voltage application, the current density stabilizes, and the displacement current ceases, allowing for a revision of Equation (12).

$$\nabla \cdot (\varepsilon_0 \varepsilon_r E) = 0 \quad (11)$$

$$\nabla \cdot J = \nabla \cdot (\sigma E) = 0 \quad (12)$$

However, Equations (11) and (12) become incompatible in the presence of variations in permittivity and conductivity, necessitating the existence of space charges in steady state for these equations to hold. This leads to a relational expression derived from combining Equations (7) and (10).

$$\nabla \cdot (\varepsilon_0 \varepsilon_r \frac{J}{\sigma}) = J \cdot \nabla (\frac{\varepsilon_0 \varepsilon_r}{\sigma}) + \frac{\varepsilon_0 \varepsilon_r}{\sigma} \nabla \cdot J = J \cdot \nabla (\frac{\varepsilon_0 \varepsilon_r}{\sigma}) = \sigma E \cdot \nabla (\frac{\varepsilon_0 \varepsilon_r}{\sigma}) = \rho \quad (13)$$

The final relational Equation (13) confirms that space charges can form if the permittivity/conductivity ratio within the dielectric varies spatially as DC current flows. Given that the dielectric constant is typically stable across a broad temperature range, it suggests that space charge formation is primarily due to conductivity changes. Thus, electric field inversion occurs due to spatial conductivity changes caused by temperature gradients within the insulation material, leading to space charge accumulation [27,28]. Finally, the governing equations of the conductivity-based model for calculating the electric field inside the HVDC cable are composed of Equations (7)–(10) described above.

The temperature calculation inside the cable relies on the heat transfer equation, as shown in Equation (14). Joule heating is represented by the heat source Q , accounting for losses in the DC cable. Cooling of the cable is assumed to be due to external convection, and this is set as the outer boundary condition of the cable, as described in Equation (15).

$$\rho_d C_p \frac{\partial T}{\partial t} = \nabla \cdot (k_c \nabla T) + Q \quad (14)$$

$$q_0 = h(T_{ext} - T) \quad (15)$$

where ρ_d represents the density of material, C_p is the heat capacity at constant pressure, k_c is the thermal conductivity, Q is the heat source from the conductor, q_0 is the heat flux, h represents the convective transfer coefficient, and T_{ext} is the external temperature.

4.2. Pressure Analysis Model for Porous Media

Porosity (ε_p) is defined as the volume fraction through which a fluid can flow within a solid material. As illustrated in Figure 4a, mass impregnated insulation involves the migration of mass oil through porous paper [16,29]. Consequently, the numerical model for internal pressure in MI cables can be described by integrating the fluid continuity equation and Darcy's law, which represent fluid flux in a porous medium, as shown in Equations (16) and (17).

$$\frac{\partial(\varepsilon_p \rho)}{\partial t} + \nabla \cdot (\rho u) = S_0 \quad (16)$$

$$u = -\frac{k_p}{\mu} \frac{dp}{dr} \quad (17)$$

where k_p is the permeability of the insulation paper, μ is the viscosity of the fluid, dp/dr is the pressure gradient, S_0 is the source term, and u is the velocity of fluid. The viscosity of the mass oil follows the Williams–Landel–Ferry (WLF), Equation (18). This viscosity varies with temperature and, in conjunction with the pressure gradient and permeability, determines the flow rate of the fluid through the impregnated insulation.

$$\mu = \mu_{WLF} \exp\left[\frac{-A_{WLF}(T - T_{WLF})}{B_{WLF} + (T - T_{WLF})}\right] \quad (18)$$

The density of a mass is described by the temperature- and pressure-dependent relationship as shown in Equation (19). Changes in density, which lead to expansion and contraction of the mass, subsequently cause the fluid to flow within the porous medium.

$$\rho_m = \rho_{m0} + \left(\frac{\partial \rho_m}{\partial T}\right)_p (T - T_0) + \left(\frac{\partial \rho_m}{\partial p}\right)_T (p - p_0) \quad (19)$$

where ρ_{m0} is the density of oil at a reference temperature T_0 and a reference pressure p_0 .

The porosity of MI cable insulation is known to be around 40%. At very low pressures, shrinkage cavities form as the mass oil undergoes a phase transition from liquid to gas. The cavities occupy the volume inside the butt gap, limiting the space available for the mass oil. Since the porosity of the medium represents the space available to the fluid, it is set to decrease linearly below the pressure level at which cavities are expected to form. This decrease in porosity also helps prevent the development of excessive negative pressure during cooling cycles, such as when the load is turned off. When the temperature distribution in the cable insulation reaches a steady state, the density change of the mass over time stabilizes, and the relocation of the mass is almost complete, resulting in a small magnitude of flow rate and a corresponding drop in internal pressure. In this state, if the density of the mass on the conductor side increases due to load-off, a very large negative pressure is required to create an inward flow velocity. However, excessively large negative pressures and pressure gradients inside the insulation are unrealistic based on measurements in the literatures [16–18]. Therefore, it is necessary to adjust the porosity

below a certain very low pressure level to moderate the rate of density change over time. The corresponding porosity change graph is shown in Figure 4b. It is assumed that below 0.02 bar, voids are formed, and at higher pressures, the porosity slightly increases due to the formation of mass films between the papers [16].

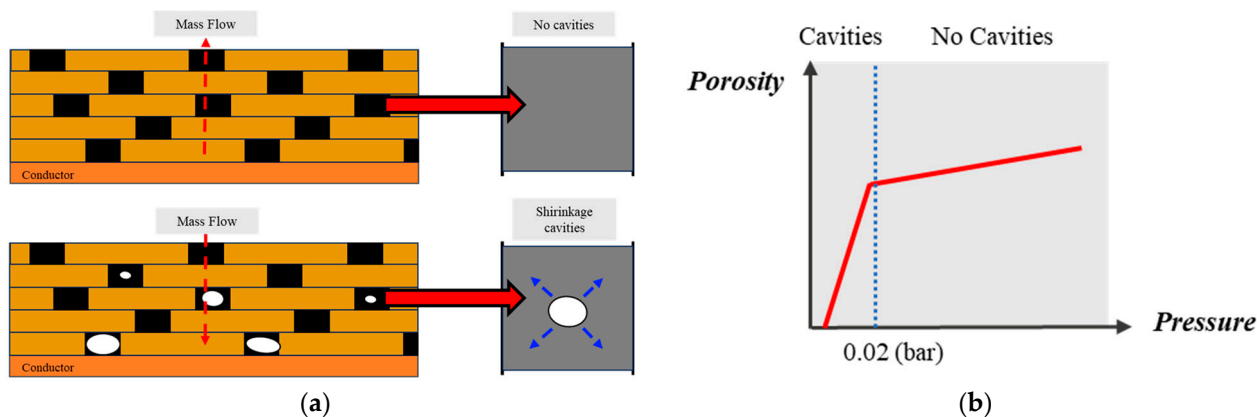


Figure 4. Considerations in pressure analysis model: (a) cavitation phenomenon within MI cables; (b) porosity changes with pressure.

4.3. Geometry and Simulation Conditions

The 500 kV HVDC MI cable model is described as a one-dimensional axisymmetric structure, designed for simplicity and clarity in simulations. All components of the cable are configured as homogeneous and isotropic materials, ensuring uniform properties throughout. To further simplify the model, the semi-conducting layer has been omitted. Detailed specifications such as cable dimensions and material properties are comprehensively listed in Tables 2 and 3.

Table 2. HVDC MI cable dimensions.

Cable Components	Radius (mm)
Copper conductor	23.15
Mass-impregnated insulation	43.7
Lead sheath	47.9
Polyethylene sheath	51.2
Steel band	52
Steel armor	58
Outer serving	63

Table 3. Material properties.

Parameters	Value
Parameters of viscosity	
μ_{WLF}	2.1 Pa·s
A_{WLF}	8.15
B_{WLF}	125 K
T_{WLF}	323 K
Density of mass (ρ_{m0})	939 kg/m ³
Pressure-dependent of density ($\partial\rho_m/\partial p$)	4.7·10 ⁻⁷ s ² /m ²
Temperature-dependent of density ($\partial\rho_m/\partial T$)	−0.6 kg/(K·m ³)

The operation of polarity reversal was detailed into several stages. Initially, the time periods for switching the load-off and back on were categorized into two scenarios: 10 days (Case I) and 20 days (Case II). Subsequently, the intervals of the load being off were set differently, and the polarity of the voltage was reversed accordingly, as depicted in Figure 5. The graph illustrates the internal pressure dynamics for 20 days after the load was switched on. It can be observed from the graph that the internal pressure has not reached a steady state by day 10, unlike on day 20.

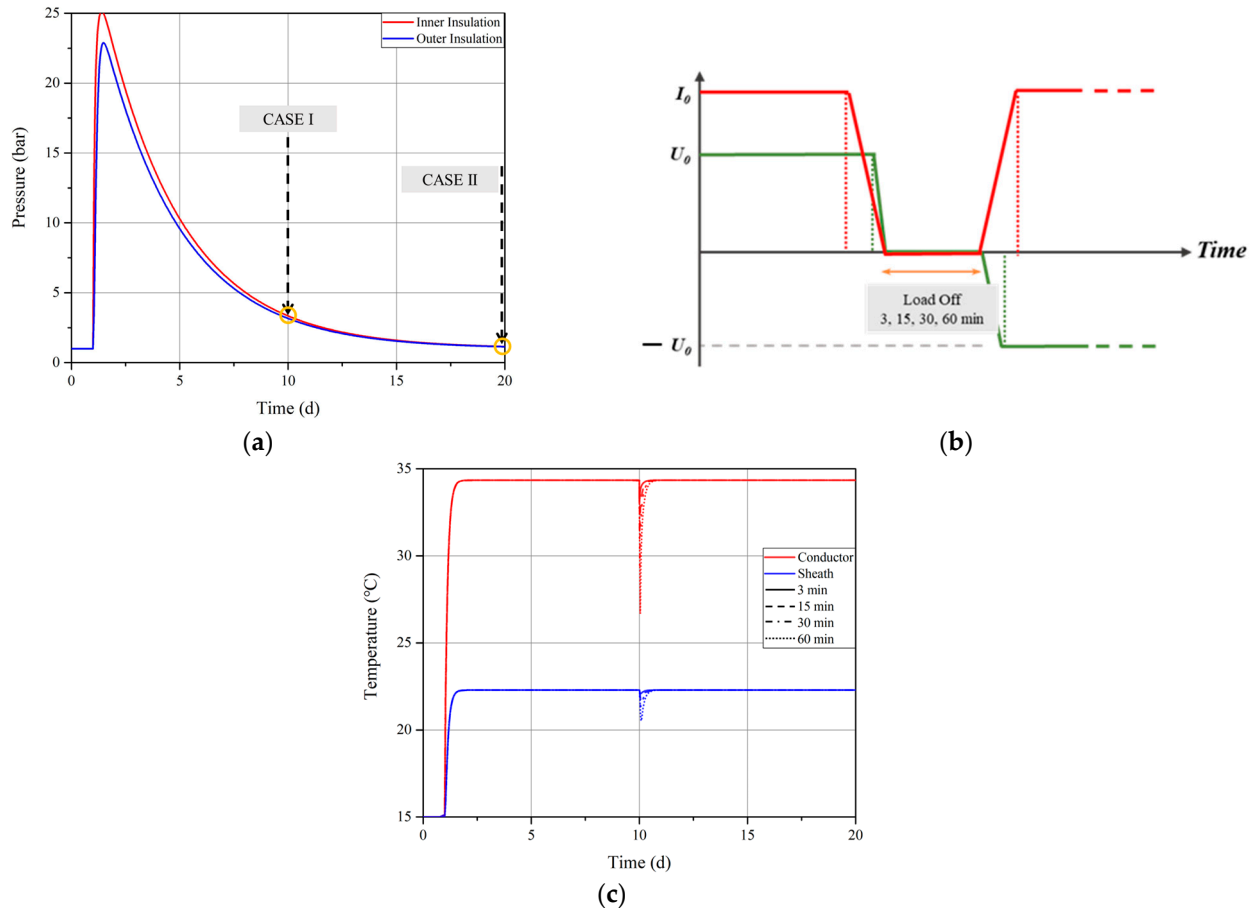


Figure 5. Simulation conditions: (a) polarity reversal time 10 days (CASE I) and 20 days (CASE II); (b) voltage and current conditions. The red and green lines represent current and voltage, respectively; (c) temperature plot on conductor and sheath side. The results for each load condition are expressed with different dotted lines.

The cable was subjected to a heat source, assuming 1400 A in the conductors, and the outside temperature was assumed to be 15 °C to facilitate natural cooling as shown in Figure 5c. When the temperature distribution within the cable stabilized, the temperature difference between the conductor and the sheath sides was approximately 12 °C. After a 60-min load-off interval, the temperatures on the conductor side and the sheath side cooled to 26.5 °C and 20.3 °C, respectively. Upon reactivating the load, the temperatures were observed to return to their previous levels. The external pressure was set at 1 bar, and the pressure and field distribution within the MI cable's inner insulation layer during load on/off and polarity reversal were derived.

5. Simulation Results and Discussion

5.1. Time-Varying Electric Field in MI Cable

Figure 6 shows the time-varying field distribution within the insulation after the initial load is turned on and subsequent polarity reversal occurs. Initially, in the absence of a temperature gradient, the maximum intensity of the capacitive field was located at the innermost layer of the insulation. As the temperature gradient developed over time, the location of the maximum field intensity shifted from the inner to the outer insulation. The differences in the coefficients of conductivity created slight variations in the electric field distribution at DC steady state. As shown in Figure 6a, in the case of aged insulation, the maximum field intensity on the outer side increased to 26.82 kV/mm, which is about 0.6 kV/mm higher than in the unaged case. Overall, the changes in the electric field distribution due to aging were not pronounced.

When the voltage was turned off, the resistive electric field formed in the DC steady state begins to decrease. However, there are still charges that remain inside the cable after the voltage is turned off, and it takes time for these charges to be rearranged. The negative electric field intensity shown in Figure 6a shows the unbalanced state of these charge carriers, which means that the charges did not disappear completely even when the voltage was turned off. At this time, if polarity reversal is performed without sufficient time, the electric field formed by the remaining space charge and the capacitive field due to the application of a negative voltage will be superimposed. The capacitive electric field is expressed by Equation (20).

$$E = \frac{U_0}{r \ln\left(\frac{r_o}{r_i}\right)} \quad (20)$$

where U_0 is the applied voltage, r represents the radius in the cable insulation, and r_0 and r_i are the outer and inner radius of insulation, respectively. The calculated capacitive field strength on the conductor side is approximately 34 kV/mm. Figure 6b shows that the field strength on the conductor side increased to 46.61 kV/mm. The strong transient electric field demonstrated in the simulation results is a consequence of the superposition of the about 13 kV/mm field present on the conductor side after the voltage is turned off, with the capacitive field induced by polarity reversal.

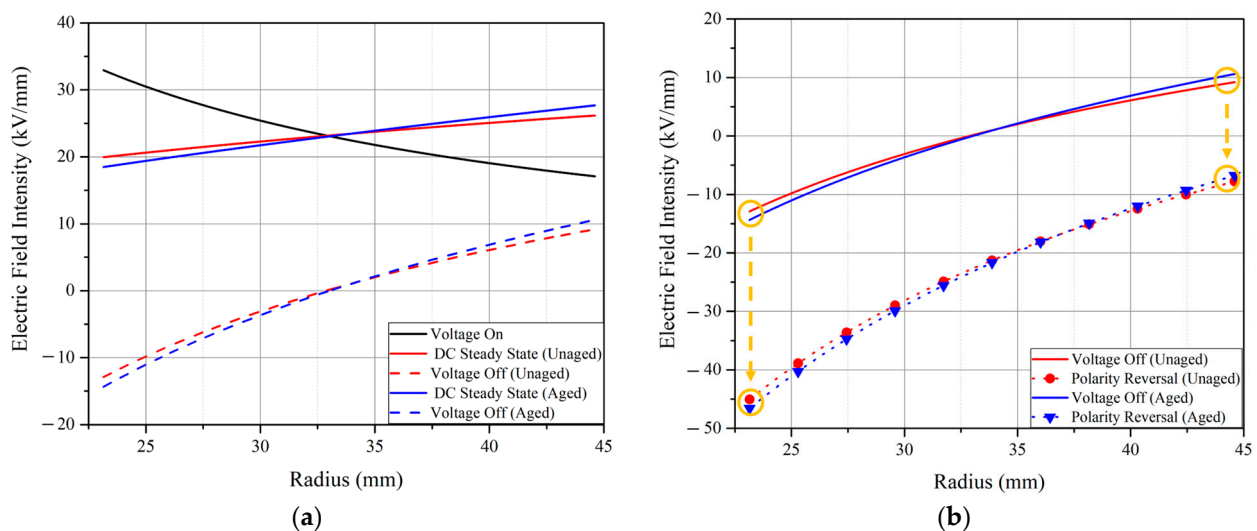


Figure 6. Time-varying electric field distribution within the insulation: (a) voltage off; (b) polarity reversal. The yellow arrows indicate the change in electric field distribution when polarity is reversed.

Figure 7 displays the electric field distribution at the polarity reversal for different load-off intervals. The maximum field intensity on the conductor side decreased to 39.18 kV/mm as the intervals increased. Naturally, extending the period during which

voltage and current are cut off can reduce the internal electric field before reversing polarity, thereby minimizing electrical stress. However, the time required to reduce the internal field can range from several hours to several days, and such operations are not typical. Consequently, since the enhancement of the field on the conductor side during polarity reversal is inevitable, it is essential to minimize internal cavitation within the insulation and prevent more localized field concentrations, not just consider the macroscopic electric field behavior.

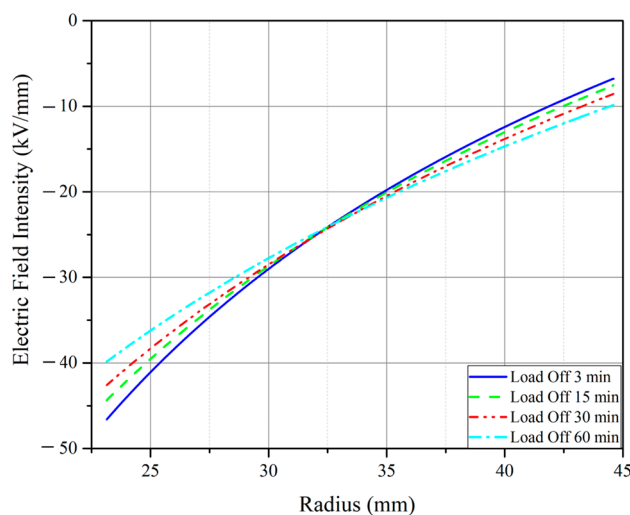


Figure 7. The electric field distribution at the polarity reversal for different load-off interval.

5.2. Internal Pressure Analysis for CASE I

The simulation results for each load-off time interval in Case I are displayed in Figure 8. Since the same Joule heating was applied, the pressure behavior before load-off was identical. The maximum pressure gradient between the inner and outer insulation was about 2.5 bar, after which the pressure gradually decreased as the temperature distribution stabilized and the redistribution of the mass was completed. The pressure in the inner insulation remained at a very low value of less than 0.02 bar for a certain period, except for a time interval of 3 min. This phenomenon indicates the formation of cavities at that location. Conversely, the pressure on the outer insulation decreases but remains above 0.02 bar.

Furthermore, the time required for the cavities to disappear increased significantly as the load-off time lengthened. As demonstrated in Figure 9, it took from a minimum of about 9 h to a maximum of about 13 days for the inner pressure to rise above 0.02 bar after cavity formation. This observation underscores that the load-off time interval significantly influences not only the likelihood of void formation but also the volume of the voids and the duration of their dissipation. In essence, the longer the load-off period, the greater the decrease in the conductor's temperature, which exacerbates the nearby mass deficit and leads to more extensive formation of shrinkage cavities. Additionally, the reduced temperature increases the viscosity of the mass, complicating the flow dynamics and necessitating very low pressures to move inward sufficiently to fill the cavities, a process further constrained by changes in porosity. Consequently, the longer the load-off time, the more time is needed for the voids to dissipate.

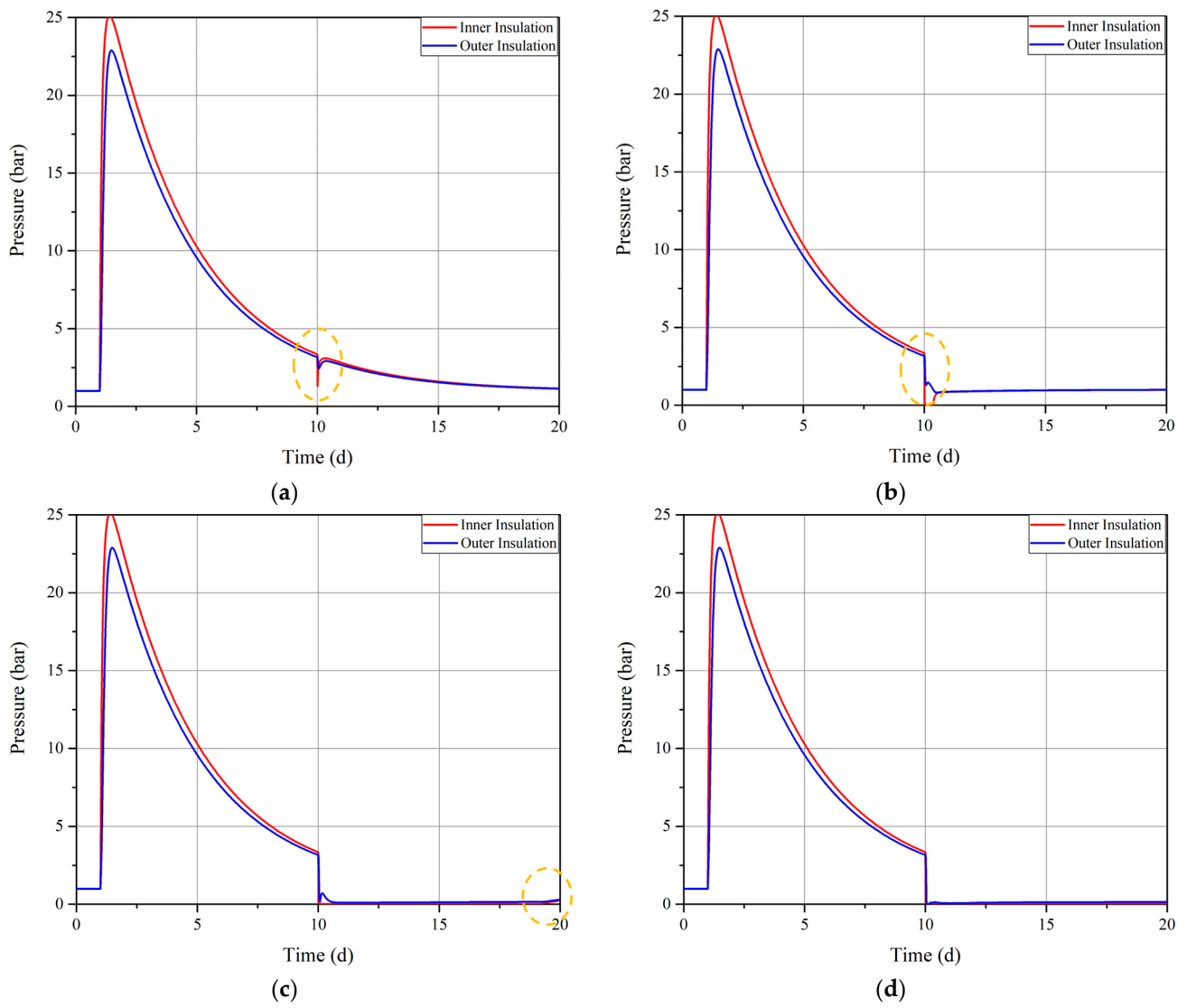


Figure 8. Internal pressure profiles within cable insulation by load-off intervals. Yellow circles indicate times to observe carefully: (a) 3 min; (b) 15 min; (c) 30 min; (d) 60 min.

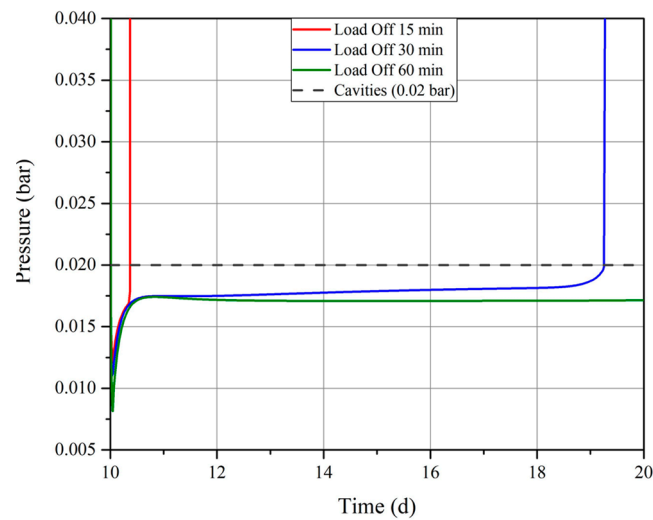


Figure 9. Internal pressure graphs at inner insulation after load-off in CASE I.

5.3. Internal Pressure Analysis for CASE II

The simulation results for each load-off time interval corresponding to CASE II are shown in Figure 10. Despite only the load-off time differing from CASE I, with all other conditions being the same, the results are notably different. In CASE II, cavities formed even with a load-off time interval of just 3 min, and they took a remarkably long time to disappear—about 7 days. For the next condition, a 15-min load-off interval, the void had not yet disappeared after 40 days, exceeding the total duration of the simulation. Consequently, the time for the cavities to fill is expected to be much longer, and simulation results for this condition are not further presented in this paper.

To investigate the reason for the differing cavity disappearance times between CASE I and CASE II, the pressure distribution inside the insulation is depicted in Figure 11. As described in the earlier simulation conditions, the internal pressure in CASE I is still decreasing, while in CASE II, it has reached a steady state with little change. Therefore, the overall magnitude of the internal pressure before the load is turned off is higher in CASE I. Since the load-off duration and the temperature change inside the cable are identical in both cases, the oil density change and the decrease in internal pressure are also the same. It is particularly noteworthy that in CASE I, the pressure does not reach the cavity-forming level after the same amount of time due to the higher initial pressure. Additionally, the pressure gradient along the radius, which is indicative of the mass flow rate, nearly disappears in the inner insulation after the cavities form, preventing backflow to fill the cavities. In conclusion, the larger initial pressure just before load-off in CASE I is crucial, as it provides a margin that prevents the pressure from dropping low enough to form cavities, accounting for the differences observed between the two simulation results.

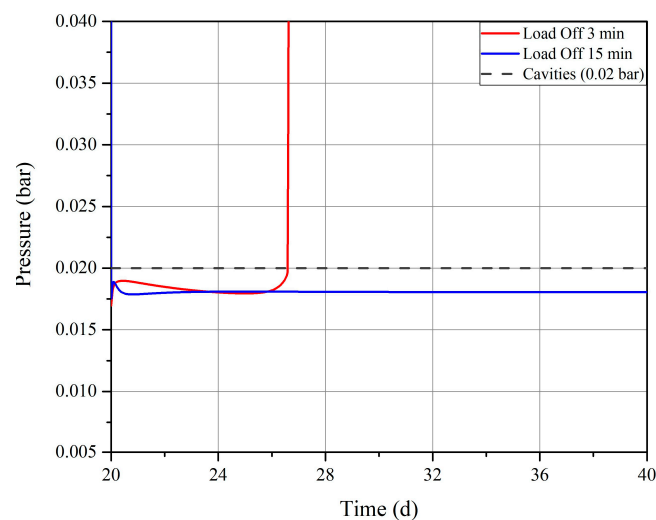


Figure 10. Internal pressure graphs at inner insulation after load-off in CASE II.

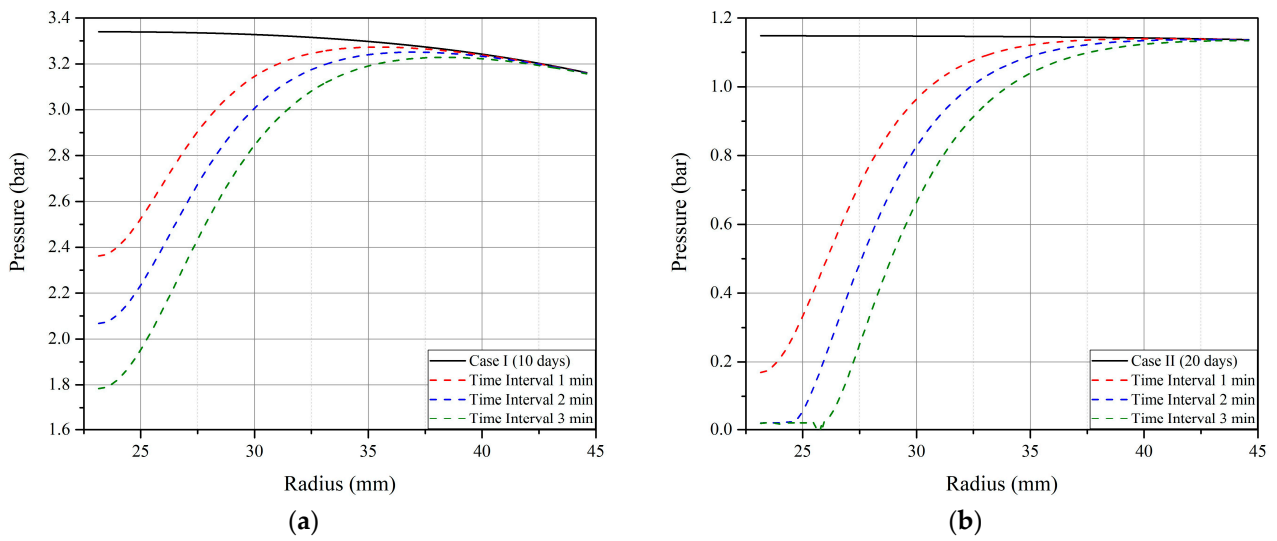


Figure 11. Internal pressure changes during load-off interval: (a) CASE I; (b) CASE II.

5.4. Adjusting Load Profiles to Prevent Cavitation

Based on previous simulation results, we adjusted the load conditions for CASE III to prevent cavitation in MI cables. CASE III was the same as CASE II, except the current was increased by 10% in the 12 h before load-off. As shown in Figure 12, the pressure on the conductor side increased to 6.5 bar and then decreased to 0.49 bar. It was found that a temporary increase in load current can help prevent cavitation, as the pressure does not drop to levels low enough to form cavities.

During polarity reversal, it is unusual to turn off the voltage for more than a few hours to reduce the overall field strength before turning it back on. Additionally, because the cable insulation is exposed to high electric fields for at least several hours after the polarity reversal, it is advisable to operate under conditions that minimize or rapidly dissipate cavity formation. Simulation results under various conditions show that the duration of the load-off period and the magnitude of the internal pressure just before the load is turned off are the most critical factors affecting the formation and disappearance of cavities in MI cables. In conclusion, for the reliable operation of MI cable systems, it is essential to adopt short load-off periods to prevent excessive cable cooling and to ensure that adequate internal pressure is maintained.

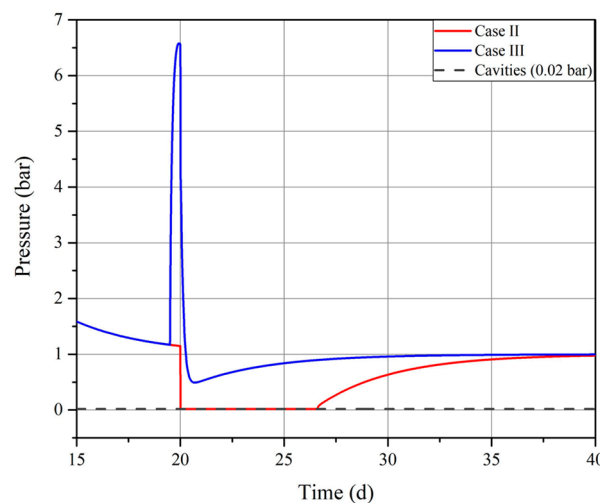


Figure 12. Internal pressure profiles at inner insulation for CASE II and CASE III.

6. Conclusions

This study has comprehensively investigated the operational challenges and degradation risks associated with aged HVDC MI cables under conditions of polarity reversal. Through experimental and simulation approaches, we have identified crucial factors influencing the integrity and performance of MI cables.

- It was confirmed that the mass-impregnated paper was resistant to thermal stress and that there was no noticeable change in electrical conductivity even after long-term deterioration.
- The time required for cavitation to dissipate increases with the load-off interval. As the temperature drops during this period, the nearby mass contracts and forms cavities, indicating that the duration of load-off is proportional to the extent of cavity formation.
- Sufficient inward migration of the mass is required to fill the shrinkage cavities created during the load-off time, but the cavities formed reduce the available space for the fluid within the porous medium. Consequently, polarity reversal is performed on the cable without adequately filling the cavities created while the cable is cooling.
- Adjustments to operational procedures, such as optimizing load conditions to reduce electrical stress and prevent excessive cooling of the cables, have been shown to effectively mitigate the risks associated with polarity reversals.

In conclusion, the research contributes to the enhancement of operational strategies for aged HVDC MI cables, ensuring reliability and extending their service life in modern power transmission networks. In future research, we aim to further refine this model and deepen our understanding of the complex phenomena in impregnated insulation systems through a broader range of experimental analyses.

Author Contributions: Conceptualization, S.-J.K. and B.-W.L.; methodology, S.-J.K.; software, S.-J.K. and S.L.; data curation, S.L. and W.-S.C.; writing—original draft preparation, S.-J.K.; writing—review and editing, S.-J.K. and S.L.; supervision, B.-W.L. All authors have read and agreed to the published version of the manuscript.

Funding: This research received no external funding.

Data Availability Statement: Data is contained within the article.

Acknowledgments: This research was supported by Korea Electric Power Corporation (grant number: R22XO05-03).

Conflicts of Interest: The authors declare no conflicts of interest.

References

1. Andersen, B. HVDC transmission-opportunities and challenges. In Proceedings of the 8th IEE International Conference on AC and DC Power Transmission, London, UK, 28–31 March 2006.
2. Arrillaga, J. *High Voltage Direct Current Transmission*; Institution of Engineering and Technology (IET): London, UK, 1998.
3. Meah, K.; Ula, S. Comparative evaluation of HVDC and HVAC transmission systems. In Proceedings of the 2007 IEEE Power Engineering Society General Meeting, Tampa, FL, USA, 24–28 June 2007; pp. 1–5.
4. Rudervall, R.; Charpentier, J.; Sharma, R. High voltage direct current (HVDC) transmission systems technology review paper. In Proceedings of the Energy Week 2000, Washington, DC, USA, 7–8 March 2000; pp. 1–19.
5. Alassi, A.; Bañales, S.; Ellabban, O.; Adam, G.; MacIver, C. HVDC transmission: Technology review, market trends and future outlook. *Renew. Sustain. Energy Rev.* **2019**, *112*, 530–554. [[CrossRef](#)]
6. Ardelean, M.; Minnebo, P. *HVDC Submarine Power Cables in the World*; Joint Research Center: Petten, The Netherlands, 2015.
7. Evenset, G.; Balog, G. *The Breakdown Mechanism of HVDC Mass-Impregnated Cables*; International Council on Large Electric Systems (CIGRÉ): Paris, France, 2000.
8. Albertini, M.; Cotugno, S.; Pietribiasi, D.; Remy, C. HPTE Extruded Cables Polarity Reversals Performance in LCC HVDC Systems. In Proceedings of the 2020 AEIT International Annual Conference (AEIT), Catania, Italy, 23–25 September 2020; pp. 1–6.
9. Wang, W.; Yan, X.; Li, S.; Zhang, L.; Ouyang, J.; Ni, X. Failure of submarine cables used in high-voltage power transmission: Characteristics, mechanisms, key issues and prospects. *IET Gener. Transm. Distrib.* **2021**, *15*, 1387–1402. [[CrossRef](#)]
10. Mazzanti, G. High voltage direct current transmission cables to help decarbonisation in Europe: Recent achievements and issues. *High Volt.* **2022**, *7*, 633–644. [[CrossRef](#)]

11. Kwak, E.-S.; Min, J.-H.; Jung, H.-C.; Moon, C.-J. A Study on HVDC and BESS Application for High Penetration of Renewable Energy Sources. *J. Korea Inst. Electron. Commun. Sci.* **2021**, *16*, 1339–1348.
12. Eriksson, A.; Henning, G.; Akke, M.; Axelsson, U. Development work concerning testing procedures of mass-impregnated HVDC cables. In Proceedings of the International Conference on Large High Voltage Electric Systems, Paris, France, 28 August–3 September 1994; pp. 21–206.
13. Runde, M.; Hegerberg, R.; Magnusson, N.; Ildstad, E.; Ytrehus, T. Cavity formation in mass-impregnated HVDC subsea cables—mechanisms and critical parameters. *IEEE Electr. Insul. Mag.* **2014**, *30*, 22–33. [[CrossRef](#)]
14. Runde, M.; Kvien, O.; Förster, H.; Magnusson, N. Cavities in mass-impregnated HVDC subsea cables studied by AC partial discharge measurements. *IEEE Trans. Dielectr. Electr. Insul.* **2019**, *26*, 913–921. [[CrossRef](#)]
15. Oh, D.-H.; Lee, H.-Y.; Kim, S.-J.; Lee, B.-W. Correlation between partial discharge inception voltage and breakdown voltage characteristics of butt-gap in HVDC mass impregnated PPLP cable. In Proceedings of the 2018 IEEE Conference on Electrical Insulation and Dielectric Phenomena (CEIDP), Cancun, Mexico, 21–24 October 2018; pp. 518–521.
16. Hestad, Ø.; Runde, M.; Enoksen, H.; Magnusson, N. Modeling of Internal Pressure Dynamics in Mass-Impregnated Nondraining HVDC Cables. *IEEE Trans. Dielectr. Electr. Insul.* **2022**, *29*, 1135–1142. [[CrossRef](#)]
17. Runde, M.; Jonsson, E.; Magnusson, N.; Solheim, K.T. Internal pressures and pressure gradients in mass-impregnated HVDC cables during current cycling. *IEEE Trans. Dielectr. Electr. Insul.* **2020**, *27*, 915–923. [[CrossRef](#)]
18. Runde, M.; Bjerrehorn, E.; Jonsson, E.; Magnusson, N. Internal pressure dynamics of mass-impregnated HVDC subsea cables at different sea depths. *CIGRÉ Sci. Eng.* **2022**, *24*, 1–11.
19. Helal, K.; Abd El-Aal, R.; Dessouky, S.; Backhaus, K.; Speck, J.; Grossmann, S. Partial discharge characteristics of a gas void embedded between oil impregnated papers under the effect of AC and DC voltage. In Proceedings of the 2018 IEEE 2nd International Conference on Dielectrics (ICD), Budapest, Hungary, 1–5 July 2018; pp. 1–4.
20. Kim, H.-S.; Oh, D.-H.; Kim, Y.-R.; Lee, B.-W. Relation between DC PDIV and DC BDV of Mass Impregnated Polypropylene Laminated Paper Considering the Thermal Aging Characteristics. In Proceedings of the 2020 8th International Conference on Condition Monitoring and Diagnosis (CMD), Phuket, Thailand, 25–28 October 2020; pp. 369–372.
21. Bystrietskaya, E.V.; Monakhova, T.V.; Ivanov, V.B. TGA application for optimising the accelerated aging conditions and predictions of thermal aging of rubber. *Polym. Test.* **2013**, *32*, 197–201. [[CrossRef](#)]
22. Dissado, L.A.; Fothergill, J.C. *Electrical Degradation and Breakdown in Polymers*; Institution of Engineering and Technology (IET): London, UK, 1992; Volume 9.
23. Setnescu, R.; Badicu, L.; Dumitran, L.; Notingher, P.; Setnescu, T. Thermal lifetime of cellulose insulation material evaluated by an activation energy based method. *Cellulose* **2014**, *21*, 823–833. [[CrossRef](#)]
24. Hampton, R. Some of the considerations for materials operating under high-voltage, direct-current stresses. *IEEE Electr. Insul. Mag.* **2008**, *24*, 5–13. [[CrossRef](#)]
25. Mauseth, F.; Haugdal, H. Electric field simulations of high voltage DC extruded cable systems. *IEEE Electr. Insul. Mag.* **2017**, *33*, 16–21. [[CrossRef](#)]
26. Reddy, C.C.; Ramu, T. On the computation of electric field and temperature distribution in HVDC cable insulation. *IEEE Trans. Dielectr. Electr. Insul.* **2006**, *13*, 1236–1244. [[CrossRef](#)]
27. Jeroense, M.; Morshuis, P. Electric fields in HVDC paper-insulated cables. *IEEE Trans. Dielectr. Electr. Insul.* **1998**, *5*, 225–236. [[CrossRef](#)]
28. Zhou, Y.; Peng, S.; Hu, J.; He, J. Polymeric insulation materials for HVDC cables: Development, challenges and future perspective. *IEEE Trans. Dielectr. Electr. Insul.* **2017**, *24*, 1308–1318. [[CrossRef](#)]
29. Szabo, P.; Hassager, O.; Strobeck, E. Modeling of pressure effects in HVDC cables. *IEEE Trans. Dielectr. Electr. Insul.* **1999**, *6*, 845–851. [[CrossRef](#)]

Disclaimer/Publisher’s Note: The statements, opinions and data contained in all publications are solely those of the individual author(s) and contributor(s) and not of MDPI and/or the editor(s). MDPI and/or the editor(s) disclaim responsibility for any injury to people or property resulting from any ideas, methods, instructions or products referred to in the content.